Available online at www.sciencedirect.com
SCIENCE DIRECT®
Journal of Computational Physics 199 (2004) 16–40
JOURNAL OF COMPUTATIONAL PHYSICS
www.elsevier.com/locate/jcp

High-order finite volume methods for viscoelastic flow problems

M. Aboubacar [a], T.N. Phillips [b,*], H.R. Tamaddon-Jahromi [a], B.A. Snigerev [b], M.F. Webster [a]

[a] *Department of Computer Science, University of Wales, Swansea, UK*
[b] *Department of Mathematics, University of Wales, Aberystwyth, UK*

Received 15 January 2003; received in revised form 5 January 2004; accepted 24 January 2004
Available online 11 March 2004

Abstract

In this paper accurate and stable finite volume schemes for solving viscoelastic flow problems are presented. Two contrasting finite volume schemes are described: a hybrid cell-vertex scheme and a pure cell-centred counterpart. Both schemes employ a time-splitting algorithm to evolve the solution through time towards steady state. In the case of the hybrid scheme, a semi-implicit formulation is employed in the momentum equation, based on the Taylor–Galerkin approach with a pressure-correction step to enforce incompressibility. The basis of the pure finite volume approach is a backward Euler scheme with a semi-Lagrangian step to treat the convection terms in the momentum and constitutive equations. Two distinct finite volume schemes are presented for solving the systems of partial differential equations describing the flow of viscoelastic fluids. The schemes are constructed to be second-order accurate in space. The issue of stability is also addressed with respect to the treatment of convection. Numerical examples are presented illustrating the performance of these schemes on some steady and transient problems that possess analytical solutions.

1. Introduction

Over the last two decades or so, the finite element method has dominated the field of computational rheology, upon which a vast body of literature exists on its application to the solution of viscoelastic flow problems (see for example [17]). However, progress in terms of increased stability for moderate values of the elasticity parameter has only been made possible by choosing appropriate mixed finite element approximation spaces and modifying the standard finite element method.

* Corresponding author. Tel.: +44-1970-622769; fax: +44-1970-622777.
E-mail address: tnp@aber.ac.uk (T.N. Phillips).

0021-9991/$ - see front matter © 2004 Elsevier Inc. All rights reserved.
doi:10.1016/j.jcp.2004.01.033

The analysis of the well-posedness of the classical velocity–pressure formulation of the Stokes problem is dependent on the satisfaction of a compatibility condition between the function spaces for velocity and pressure. The satisfaction of the compatibility condition, which is sometimes referred to as the inf–sup or Ladyzhenskaya–Babuška–Brezzi (LBB) condition, is necessary to ensure the existence of a unique solution for the pressure. For the three fields formulation of the Stokes problem in terms of velocity, pressure and extra-stress an additional condition must be satisfied between the function spaces for velocity and extra-stress to ensure a well-posed problem. Evidence for this was first discovered in a paper of Marchal and Crochet [14] in which they showed that the velocity–pressure and velocity–pressure–stress formulations of the Stokes problem generated different results unless the stress approximation was chosen correctly within the Galerkin formulation. For the upper-convected Maxwell (UCM) model, Fortin and Pierre [7] have shown that a second compatibility condition has to be satisfied in order to ensure the stability of the discretisation. A sufficient condition for stability is that the extra-stress space contains the gradient of the velocity space. A consequence of an incompatible selection of approximation spaces is that the velocity field may be polluted by spurious oscillations.

A theoretical analysis of standard Galerkin finite element methods has established that they are optimal for self-adjoint problems in the sense that the discretisation error is bounded by the error in the best approximation of the solution by functions in the trial space. Therefore, standard Galerkin finite element methods are ideal for the discretisation of diffusion problems. However, for convection-dominated convection–diffusion equations, which assume the character of hyperbolic problems, the best approximation property is lost. Furthermore, if the solution to the problem is nonsmooth, the Galerkin approximation becomes polluted by spurious oscillations that propagate globally. Such oscillations are not a feature of the actual solution itself. Oscillations appear when the value of the mesh Péclet number is high or when the finite element discretisation is too coarse to resolve sharp phenomena, such as boundary layers, and result from a lack of stability of the standard Galerkin finite element approach, when used to solve convection-dominated problems. The Galerkin finite element method may be stabilised using techniques such as SU or SUPG, for example. However, this increased stability is gained often at the expense of deterioration in accuracy.

Standard Galerkin methods behave in a similar fashion when the convective terms in the constitutive equation dominate. The governing equations for fluids of Maxwell/Oldroyd type are known to be of mixed type. For example, the quasilinear system of partial differential equations for the upper-convected Maxwell model is of mixed elliptic–hyperbolic type [17]. Hence, optimality in the approximation via Galerkin methods is destroyed for this class of problems. Some reformulations of the governing equation have enhanced stability for finite element calculations. Among these strategies are the elastic-viscous split-stress (EVSS) [20] and discrete EVSS (DEVSS) [9] formulations, which seek to enhance the elliptic character of the momentum equation directly. Nevertheless, the finite element method does carry with it a heavy computational overhead for complex problems. This may be conveyed through additional considerations, such as, upwinding, or increased degrees of freedom associated with different formulations. Today, it is fairly well-accepted that standard finite element methods may not be the most appropriate means by which to resolve hyperbolic equations. The objective of the current study is to devise alternative procedures for this class of problems, attending to deficiencies highlighted above, and identifying superior scheme properties as they arise.

The present *hybrid scheme* is based on a finite element discretisation of the conservation equations and a finite volume discretisation of the constitutive equation. The finite element grid is used as a platform for the finite volume grid from which control volumes are constructed. Each finite volume cell is one of four subtriangles formed by connecting the mid-side nodes of the parent element (see Fig. 1(a) in Section 3). This gives rise to a stable approximation for viscoelastic flow, close in philosophy to the so-called 4×4 stress subelements, introduced by Marchal and Crochet [14]. Here, fluctuation distribution (FD) schemes are used to distribute the flux and source residuals to the vertices of each finite

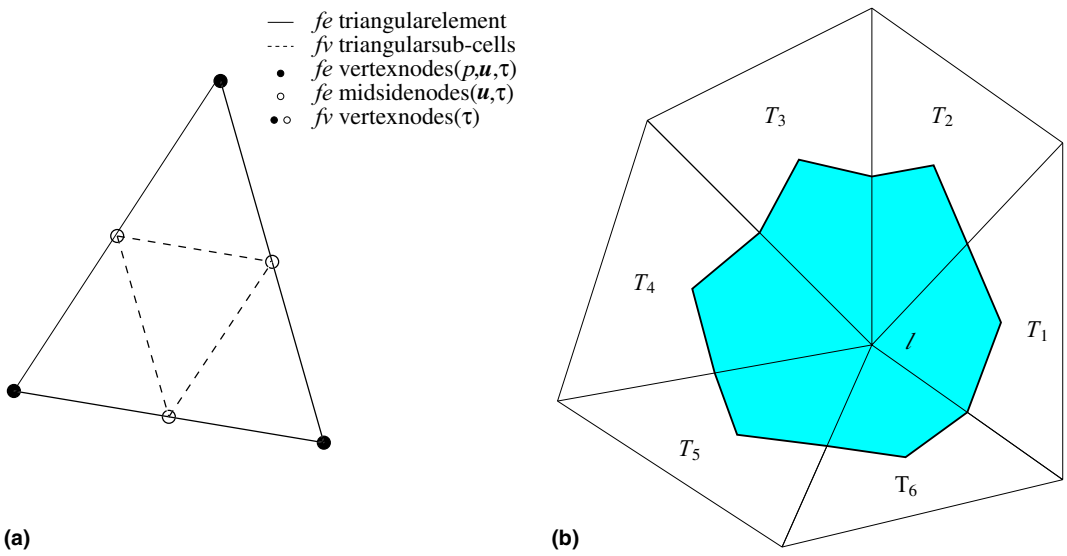

Fig. 1. Spatial discretisation: (a) FE-cell with four FV-subcells and (b) FV control volume for node l with median-dual-cell (shaded).

volume triangle. FD schemes can be constructed to possess certain advantageous properties. For example, on each control volume, all such schemes satisfy conservation of the convected quantity in question. In addition, the linear FD scheme presented here, the low-diffusion B (LDB) scheme, is linearity preserving (second-order accurate in space for linear solutions). High-order accuracy is achieved through a consistent treatment of flux and source terms in the constitutive equation. Enhanced stability, with respect to larger Weissenberg number attainment, is realised by inclusion of contributions from flux and source terms, based on the median-dual-cell construct (MDC). This is paramount to ensure stability in convergence for complex flows. A generalised finite volume nodal-update is proposed, including additional consideration for time-term discretisation.

In contrast, the main features of the *pure finite volume scheme* correspond to those extracted on a staggered grid arrangement for the unknowns and a semi-Lagrangian treatment for convection terms of momentum and constitutive equations. The discrete equations are solved through a generalisation of the SIMPLER scheme, enhanced to include the constitutive equation. The semi-Lagrangian component of the computation utilises interpolation based on area-weighting. Second-order area-weighting is employed, developed by Phillips and Williams [18] for conservation laws and implemented in the context of Newtonian computational fluid dynamics. A first-order variant of this scheme has already been established for complex flows [19]. This scheme is inherently conservative, when applied to conservation laws, and leads to a stable scheme. It circumvents the problems associated with high-order upwinding schemes, traditionally introduced into some finite volume schemes.

There are two different forms of mesh arrangement proposed in conjunction with cell-centred finite volume schemes for viscoelastic flows. On the first, all components of the extra-stress tensor are located at the centre of mesh cells. This approach has been used by Yoo and Na [29], Sasmal [21] and Xue et al. [28]. This arrangement has the advantage of not having an unknown located at a cell vertex, that may correspond to a singularity in the solution. Nevertheless, such a configuration of unknowns has the disadvantage of requiring interpolation of shear stress values, for inclusion within the discrete representation of the momentum equation. On the second grid arrangement, which is adopted in this paper, the shear stress is located at the corners of mesh cells. The normal stress components are located at the same positions as the

pressure, that is at the centre of mesh cells. Such an arrangement has been used by Bevis et al. [2], Gerritsma [8] and Mompean and Deville [15].

Both finite volume schemes are validated on model steady and transient viscoelastic problems to demonstrate spatial and temporal accuracy. The steady problem is a two-dimensional Cartesian test problem in which the velocity field is specified. The transient problem is the classical problem of start-up Poiseuille flow in a channel, in which the inflow conditions are known analytically, from Waters and King [25]. This is a transient shear flow, so inertia is negligible. Here, one may attempt to reproduce the transient evolution of velocity and/or stress, and compare the same against the corresponding theoretical solution.

2. Governing equations

The governing equations comprise the conservation equations of momentum and mass, together with the rheological equation of state for an Oldroyd-B fluid. In dimensionless form, the equations of motion and continuity read

$$Re\left(\frac{\partial \mathbf{u}}{\partial t}+\mathbf{u}\cdot\nabla\mathbf{u}\right)=-\nabla p+\nabla\cdot\boldsymbol{\tau}+\nabla\cdot(\beta(\nabla\boldsymbol{u}+(\nabla\boldsymbol{u})^{\mathrm{T}})), \tag{1}$$

$$\nabla\cdot\mathbf{u}=0, \tag{2}$$

where Re is the Reynolds number, p is an arbitrary isotropic pressure, $\boldsymbol{\tau}$ is the polymeric contribution to the extra-stress tensor and $\mathbf{u}$ is the velocity vector. The parameter β, the solvent to total viscosity ratio, is defined by

$$\beta=\frac{\lambda_2}{\lambda_1}, \tag{3}$$

expresses the ratio between the retardation and relaxation times of the fluid in question. The dimensionless form of the Oldroyd-B model may be represented as

$$\boldsymbol{\tau}+We\overset{\triangledown}{\boldsymbol{\tau}}=2(1-\beta)\mathbf{D}, \tag{4}$$

where $\overset{\triangledown}{\boldsymbol{\tau}}$ is the upper-convected derivative of $\boldsymbol{\tau}$, defined by

$$\overset{\triangledown}{\boldsymbol{\tau}}=\frac{\partial\boldsymbol{\tau}}{\partial t}+\mathbf{u}\cdot\nabla\boldsymbol{\tau}-(\nabla\mathbf{u})^{\mathrm{T}}\cdot\boldsymbol{\tau}+\boldsymbol{\tau}\cdot(\nabla\mathbf{u}), \tag{5}$$

the rate of deformation tensor $\mathbf{D}$ is defined by

$$\mathbf{D}=\frac{1}{2}(\nabla\mathbf{u}+\nabla\mathbf{u}^{\mathrm{T}}), \tag{6}$$

and We is the Weisenberg number. The Reynolds and Weissenberg numbers are defined by

$$Re=\frac{\rho UL}{\eta},\quad We=\frac{\lambda_1 U}{L}, \tag{7}$$

where ρ is the density, η is the viscosity, U is a characteristic speed and L is a characteristic length. The extra-stress tensor, $\mathbf{T}$, is given by

$$\mathbf{T}=\boldsymbol{\tau}+2\beta\mathbf{D}. \tag{8}$$

Note that $\beta = 0$ corresponds to the UCM model. In this instance, there is no solvent contribution to the extra-stress tensor and no diffusion term in (1). The governing equations become increasingly more resilient to solution (stiffer) as values of β tend to zero.

The value of the parameter β is normally taken to be $1/9$ in numerical simulations. This is the smallest value of this parameter that ensures the shear stress is a monotonically increasing function of shear rate for the Johnson–Segalman model, of which the Oldroyd-B model is a special case. Although this lower bound on the value of β is not directly relevant for the Oldroyd-B model, it is the value often adopted in the majority of numerical simulations. One notes that, in order to reflect quantitative comparisons with experiments on materials such as Boger fluids, the value of β should be taken as at least 0.9.

3. Hybrid FE/FV schemes

The present hybrid finite element/volume method (FE/FV) is based upon a time-splitting semi-implicit formulation. The latter consists of a Taylor–Galerkin scheme and a pressure-correction scheme. The Taylor–Galerkin scheme (predictor–corrector) features a two-step Lax-Wendroff time-stepping procedure, that is extracted via a Taylor series expansion in time [6,30]. The pressure-correction method handles the incompressibility constraint to ensure second-order accuracy in time [10,13]. This formulation leads to a three-stage structure, for each time-step cycle. The emerging discrete system can be expressed in matrix–vector notation [24] as follows:

$$
\begin{aligned}
&\text{Stage 1a}\\
&\quad \frac{2}{\Delta t} A_u(\mathscr{U}^{n+1/2} - \mathscr{U}^n) = b_u(\mathscr{P}^n, \mathscr{U}^n, \mathscr{T}^n, \mathscr{D}^n),\\
&\quad \frac{2We}{\Delta t} A_\tau(\mathscr{T}^{n+1/2} - \mathscr{T}^n) = b_\tau(\mathscr{U}^n, \mathscr{T}^n, \mathscr{D}^n),\\
&\text{Stage 1b}\\
&\quad \frac{1}{\Delta t} A_u(\mathscr{U}^* - \mathscr{U}^n) = b_u(\mathscr{P}^n, \mathscr{U}^n, \mathscr{U}^{n+1/2}, \mathscr{T}^{n+1/2}, \mathscr{D}^{n+1/2}),\\
&\quad \frac{We}{\Delta t} A_\tau(\mathscr{T}^{n+1} - \mathscr{T}^n) = b_\tau(\mathscr{U}^{n+1/2}, \mathscr{T}^{n+1/2}, \mathscr{D}^{n+1/2}),\\
&\text{Stage 2}\\
&\quad \frac{\Delta t}{2} A_2(\mathscr{P}^{n+1} - \mathscr{P}^n) = b_2(\mathscr{U}^*),\\
&\text{Stage 3}\\
&\quad \frac{2}{\Delta t} A_3(\mathscr{U}^{n+1} - \mathscr{U}^*) = b_3(\mathscr{P}^n, \mathscr{P}^{n+1}).
\end{aligned}
\tag{9}
$$

where $\mathscr{U}, \mathscr{U}^*, \mathscr{P}, \mathscr{T}, \mathscr{D}$ represent nodal values for velocity, non-solenoidal velocity, pressure, extra-stress and velocity gradient, respectively. The superscript n denotes time level, and Δt the time step. The matrices A_u, A_τ, A_2, A_3 correspond to system matrices for momentum, stress and stage 2, 3 equations, respectively, with their rhs-equivalents in b_k. For a pure FE implementation, all three stages are discretised via a Galerkin formulation. This results in augmented Galerkin mass matrix–vector equations for stage 1 (momentum and stress constitutive equations) and stage 3 (incompressibility constraint). An efficient element-by-element Jacobi scheme is invoked to solve for these stages. This is an extremely efficient scheme that typically requires at most five iterations to attain the required convergence criterion. Note that a consistent matrix is used in the predictor stage to preserve the accuracy of the scheme and that the diffusion

term in the momentum equation is treated in a semi-implicit fashion to enhance stability. The pressure-correction (stage 2), which satisfies a Poisson equation, is handled via a direct Choleski decomposition procedure. Note that the reduction phase in this decomposition only has to be performed once.

For the *hybrid* FE/FV implementation, the momentum equations at stage 1 are treated in the same manner, as described above for a pure FE approach. The same is true for stage 2 and stage 3. Only the treatment of the stress constitutive equation differentiates the two approaches. In the hybrid scheme, A_τ is the identity matrix (as opposed to a sparse Galerkin form for pure FE). Consequently, the need to resolve a matrix–vector equation is avoided. In addition, the rhs (b_τ) is discretised through a combination of cell-vertex FD- and MDC constructs. These two characteristics of the hybrid method (identity A_τ and straightforward b_τ) reduce memory overhead and ensure a lower computational burden per time-cycle, over the pure FE instance. The computational domain is discretised using six-noded FE-triangular cells, composed of three vertices and three mid-side nodes (Fig. 1(a)). Velocity components are interpolated via quadratic shape functions, based upon the six nodal-values of the FE-triangle. In contrast, pressure is represented in a linear fashion, based on the FE vertices nodal-values alone. Stress interpolation (FV-subcell) is of linear form, with an associated non-recovered stress gradient (non-conservative form). Note, the finite volume tessellation is embedded within the parent FE-grid, by connecting the mid-side nodes of each parent FE-cell (Fig. 1(a)). This generates four FV-triangular subcells, upon which stress components are computed (see next section). The FV-subcell discretisation mitigates propagation errors, when recovering stress nodal-values, as required by reference within the momentum equation approximation.

3.1. Cell-vertex finite volume stress discretisation

We appeal to cell-vertex FD schemes to split the discrete flux (R) and source (Q) residuals to the vertices of each FV-subtriangle T. Originally, such upwinding-schemes were designed in the context of pure advection problems [5,11,12,16]. These FD schemes possess such properties as conservation, linearity preservation and/or positivity. In the viscoelastic context, our experience suggests that linearity preservation is paramount to ensure accurate results. This is true in both transient and steady-state regimes. In contrast, positivity has been observed to improve the quality of solution representation at short times, yet, at long-times and towards steady state, the situation somewhat deteriorates. This indicates that positivity must be handled with care in the presence of complex (solution-dependent) source terms. Hence, we retain the low-diffusion B (LDB) FD scheme for the present hybrid fv implementation: a linear scheme, with the linearity-preserving property. Detailed discussion on these issues can be found elsewhere [23].

To obtain the discrete flux and source terms, we isolate their continuous counterparts ($\mathscr{R}$ and $\boldsymbol{Q}$) in the stress constitutive equation, viz.

$$\frac{\partial \boldsymbol{\tau}}{\partial t} = -\mathscr{R} + \boldsymbol{Q}, \tag{10}$$

$$\mathscr{R} = \boldsymbol{u} \cdot \nabla \boldsymbol{\tau}, \tag{11}$$

$$\boldsymbol{Q} = \frac{1}{We}[2(1-\beta)\boldsymbol{d} - \boldsymbol{\tau}] + \boldsymbol{L} \cdot \boldsymbol{\tau} + \boldsymbol{\tau} \cdot \boldsymbol{L}^{\mathrm{T}}. \tag{12}$$

Assuming appropriate spatial representation, integrating Eqs. (10)–(12) over suitable control volumes, for each scalar stress component, τ, provides the necessary time, flux and source discrete residuals:

$$\int_{\Omega_I} \frac{\partial \tau}{\partial t} \, \mathrm{d}\Omega = \int_{\Omega_T} \boldsymbol{u} \cdot \nabla \tau \, \mathrm{d}\Omega + \int_{\Omega_I} Q \, \mathrm{d}\Omega. \tag{13}$$

In the present FV implementation, we use two such control volumes: the FV-triangle T and the MDC [1] control volume (Fig. 1(b)). The triangle T provides the flux and source (R_T, Q_T) to be distributed via a given FD strategy (here, LDB). In addition, we appeal to the MDC, which is uniquely identified with a given node l within the FV-cell T. This introduces additional flux and source terms, $(R^l_{\mathrm{MDC}^T}, Q^l_{\mathrm{MDC}^T})$, respectively. Judicious combinations of these different residuals leads to optimal stress nodal-update equations, as we proceed to demonstrate.

Departing from pure-advection problems (R_T only), a standard extension of cell-vertex FD-nodal-update for node l appends source Q_{MDC}, via

$$\frac{\hat{\Omega}_l}{\Delta t}(\tau_l^{n+1} - \tau_l^n) = \sum_{\forall T} \alpha_l^T R_T + \sum_{\forall T} Q^l_{\mathrm{MDC}^T}. \tag{14}$$

Here, $\sum_{\forall T}$ represents all contributions from FV-cells (T) surrounding node l. The flux R_T is split between the FV-subcell vertices through the FD coefficients α_l^T (see on for definition). We note, flux R_T and source $Q^l_{\mathrm{MDC}^T}$ terms are evaluated over different control volumes. As such, we denote this strategy as ''inconsistent''. Indeed, this standard approach provides inaccurate results, even for simple model problems (steady sink flow [4] and channel flow [24], with the Oldroyd-B model). As a consequence, a consistent approach has been proposed by Wapperom and Webster [24]. With this formulation, both flux and source terms are calculated over the same control volume, and distributed together, via factors α_l^T:

$$\frac{\hat{\Omega}_l}{\Delta t}(\tau_l^{n+1} - \tau_l^n) = \sum_{\forall T} \alpha_l^T (R_T + Q_T). \tag{15}$$

The difference between (14) and (15) lies in the control volume area of reference for Q_T. In (15), the full finite volume triangular cell is used to compute the contribution to the source term, whereas in (14) the MDC is used. The consistent approach based on (15) has performed well. It has provided second-order accurate results for the aforementioned steady-state problems: sink flow [4] and Cartesian test problems [27]. Unfortunately, such schemes lack stability. For example, the consistent approach was unable to reach a converged steady-state solution beyond $We = 1$ for the channel flow [24], a pure shear flow. This was alleviated by the addition of a consistent MDC contribution to Eq. (15) [24]. Aboubacar and Webster [1] went further, with CT2-scheme, to include consistent area-weighting for fluctuation-distributioned and MDC terms. This, in turn, enhanced stability significantly in complex flows (attaining levels of $We \approx \mathrm{O}(3)$ on highly refined meshes for the benchmark 4:1 contraction flow of an Oldroyd-B model fluid [1]).

Recently, Webster and coworkers [23] have generalised these formulations to resolve transient viscoelastic flows. The starting point is to consider separately the FD and MDC contributions to the nodal update. For a single FV-subcell T_i (area Ω_{T_i}) and a given node l in T_i (with associated MDC_l subarea $\Omega_l^{T_i}$), these segregated contributions read

$$\frac{\Omega_{T_i}}{\Delta t}\alpha_l^T \left[\Delta\tau^{n+1}\right]_l = \alpha_l^T (R_T + Q_T) \quad \text{on } \Omega_{T_i}, \tag{16}$$

and

$$\frac{\Omega_l^{T_i}}{\Delta t}\left[\Delta\tau^{n+1}\right]_l = (R_{\mathrm{MDC}} + Q_{\mathrm{MDC}})^l \quad \text{on } \mathrm{MDC}_l. \tag{17}$$

[1] MDC with zones are unique non-overlapping per node l, $\hat{\Omega}_l$ an area one third of the triangular cell over which it is constructed. A MDC tessellation is equivalent to the Dirichlet tessellation/Voronoi region if the triangulation is of Delaunay form [26].

Note that the left-hand side of (16) is the result of a computation over a full, yet single FV-subcell with weighting factor α_l^T. Blending equations (16) and (17) with parameters δ_T and δ_{MDC}, and summing over all FV-subcells surrounding node l yields the present CT3-scheme

$$[\Omega_{\mathrm{FD}} + \Omega_{\mathrm{MDC}}]\frac{\Delta\tau_l^{n+1}}{\Delta t} = \underbrace{\sum_{\forall T_l} \delta_T \alpha_l^T b_T}_{\mathrm{FD}} + \underbrace{\sum_{\forall \mathrm{MDC}_l} \delta_{\mathrm{MDC}}^T b_{\mathrm{MDC}}^l}_{\mathrm{MDC}}, \tag{18}$$

where $b_T = (R_T + Q_T)$, $b_{\mathrm{MDC}}^l = (R_{\mathrm{MDC}} + Q_{\mathrm{MDC}})^l$, $\Omega_{\mathrm{FD}} = \sum_{T_l} \delta_T \alpha_l^T \Omega_{T_i}$ and $\Omega_{\mathrm{MDC}} = \sum_{\mathrm{MDC}_l} \delta_{\mathrm{MDC}}^T \Omega_l^{T_i}$. Theoretically, δ_T and δ_{MDC} are mutually linked and complementarily exclusive. We note, if we recast Eq. (18) as

$$\frac{\Delta\tau_l^{n+1}}{\Delta t} = \frac{\sum_{\forall T_l} \delta_T \alpha_l^T b^T}{\Omega_1} + \frac{\sum_{\forall \mathrm{MDC}_l} \delta_{\mathrm{MDC}}^T b_{\mathrm{MDC}}^l}{\Omega_2}, \tag{19}$$

we obtain CT3-schemes by setting $\Omega_1 = \Omega_2 \equiv \Omega_{\mathrm{FD}} + \Omega_{\mathrm{MDC}}$; alternatively, we can recover CT2-schemes [2] [1] with the combination $\Omega_1 = \Omega_{\mathrm{FD}}$ and $\Omega_2 = \Omega_{\mathrm{MDC}}$, whilst the original nodal-update (CT0) of [24] would correspond to $\Omega_1 = \Omega_2 \equiv \hat{\Omega}_l$. In [24], Wapperom and Webster defined $\delta_T = \xi/3$ if $|\xi| \leqslant 3$ and 1 otherwise, and $\delta_{\mathrm{MDC}} = 1$. There, $\xi = We(a/h)$, with a the magnitude of the advection velocity per FV-cell and h the square-root of the area of the FV-cell in question.

With the above parameter combinations, both CT2 and CT0 variants have proved inadequate in tracking transient solution evolution in a start-up planar Poiseuille flow [23]. There, significant improvement in transient accuracy was achieved with CT2-schemes by appealing to a dynamic δ_{MDC} factor, in the form $\delta_{\mathrm{MDC}} = 1 - \delta_T$. This simply recognises the complementary nature of the relative strength between flux (better discretised through FD, δ_T-weight) and source terms (optimally represented via MDC, δ_{MDC}-weight). The dependence of δ_T upon local averaged-velocity provides an estimate of the local flux-magnitude. In contrast, the CT3-scheme is relatively insensitive to the dynamic setting of δ_{MDC} for this shear flow problem, being well-reproduced with the full inclusion of MDC contribution ($\delta_{\mathrm{MDC}} = 1$). This is a clear indication of the superior consistency in the formal derivation of the CT3 scheme. Indeed, the CT3-scheme encompasses consistent control-volumes for flux and source terms on the rhs, and consistent area-weighting for the time-terms on the lhs of the equations.

In the present work, we propose an alternative definition of the δ_T-parameter, ($\delta_{\mathrm{MDC}} = 1 - \delta_T$) in the form

$$\delta_T = |R_T|/(|R_T| + |Q_T|), \tag{20}$$

so that, by default

$$\delta_{\mathrm{MDC}} = |Q_T|/(|R_T| + |Q_T|). \tag{21}$$

This definition presents several advantages over the original Wapperom and Webster [24] form. *First*, it appeals explicitly to the relative strength between local flux and source terms. *Second*, there is no need for arbitrary truncation, since the hyperbolic function employed guarantees a monotonic decrease of δ_T from unity to zero, in asymptotic fashion. Most importantly, such direct recourse to the ratio between flux and source terms over the same control volume renders the δ_T-parameter independent of mesh size. It is interesting to note that $\delta_T = \delta_{\mathrm{MDC}} = 1/2$ when $|R_T| = |Q_T|$.

[2] This form, with $\Omega_1 = \Omega_{\mathrm{FD}} = \sum_{T_l} \alpha_l^T \Omega_{T_i}$ bears close resemblance to that proposed by Hubbard and Roe [11] for pure convection flows.

4. Semi-Lagrangian finite volume schemes

The finite volume method is generally applied to a system of equations written in conservative form. Here we consider cell-centred finite volume methods for discretising the governing equations. Each of the governing equations (1), (2) and (4) is written using the following general conservative form:

$$\delta\frac{\partial\phi}{\partial t}+\frac{\partial}{\partial x}\left(u\phi\theta-\Gamma\frac{\partial\phi}{\partial x}\right)+\frac{\partial}{\partial y}\left(v\phi\theta-\Gamma\frac{\partial\phi}{\partial y}\right)=S_\phi \tag{22}$$

for Cartesian coordinates, where δ, θ and Γ are constants, and ϕ and S_ϕ are functions that are defined in Phillips and Williams [19]. Interpolation based on area-weighting techniques is used in the semi-Lagrangian part of the computation. Phillips and Williams [19] employed a first-order area-weighting scheme in their study of viscoelastic contraction flows. A second-order scheme was developed by Phillips and Williams [18] for conservation laws. In the present paper this scheme is applied for the first time to a problem in computational non-Newtonian fluid mechanics.

4.1. The computational grid

A reference grid (which remains fixed in space for all time) is placed on top of the computational domain and a control volume is associated with each unknown on the grid. In this paper the sides of each control volume are aligned with the coordinate axes. Each component of Eq. (22) is integrated over an appropriate control volume. In the finite volume formulation mass and momentum are conserved over every control volume and therefore over the whole computational domain.

A staggered grid is used in which the dependent variables are located at different points as shown in Fig. 2. This mesh ensures that the solution is not polluted by the spurious pressure modes which may be present on collocated meshes unless care is taken. However, this arrangement does introduce a shear stress variable at the corner singularity which requires special treatment.

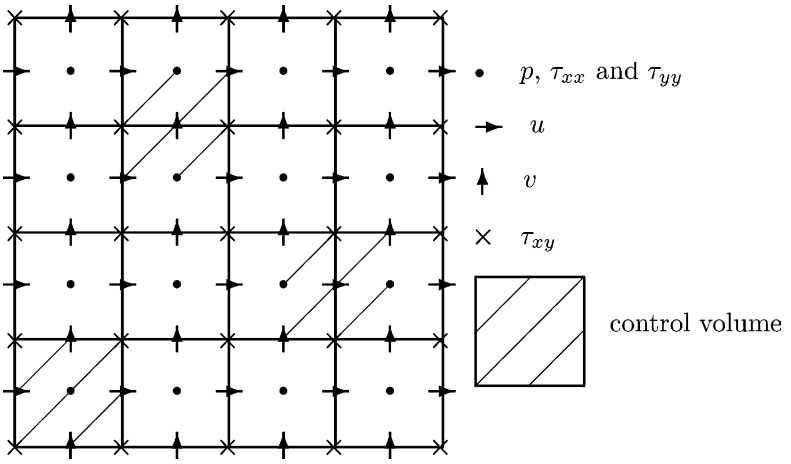

Fig. 2. Location of the variables on the finite volume grid. The shear stress is located at the vertices of the control volumes.

4.2. Discretisation

An operator splitting technique is used to discretise the governing equations in time. The convection terms in the momentum and constitutive equations are treated using a semi-Lagrangian technique based on a particle tracking method. This involves the solution of the convection problems

$$\frac{\partial \mathbf{u}}{\partial t} + \mathbf{u} \cdot \nabla \mathbf{u} = 0, \tag{23}$$

$$\frac{\partial \boldsymbol{\tau}}{\partial t} + \mathbf{u} \cdot \nabla \boldsymbol{\tau} = 0, \tag{24}$$

at each time step to obtain intermediate values of the velocity ($\mathbf{u}^*$) and extra-stress ($\boldsymbol{\tau}^*$). This is followed by the solution of an unsteady generalised Stokes problem to determine the pressure and the new velocity

$$Re\left(\frac{\mathbf{u}^{n+1} - \mathbf{u}^{*n}}{\Delta t}\right) - \beta \nabla^2 \mathbf{u}^{n+1} + \nabla p^{n+1} = \nabla \cdot \boldsymbol{\tau}^n, \tag{25}$$

$$\nabla \cdot \mathbf{u}^{n+1} = 0, \tag{26}$$

and the solution of an algebraic problem to update the stress

$$We\left(\frac{\boldsymbol{\tau}^{n+1} - \boldsymbol{\tau}^{*n}}{\Delta t}\right) - \boldsymbol{\kappa}^n \boldsymbol{\tau}^{n+1} - \boldsymbol{\tau}^{n+1} (\boldsymbol{\kappa}^n)^T + \boldsymbol{\tau}^{n+1} = 2(1-\beta)\mathbf{D}^n, \tag{27}$$

where $\boldsymbol{\kappa}$ is the transpose of the velocity-gradient tensor.

4.3. Treatment of convection

The treatment of the convection terms in (25) or (27) using a semi-Lagrangian method was described in Phillips and Williams [19]. The reader is referred to this article for further details. However, the principal components of this method are summarised here for the sake of completeness.

Consider the mesh associated with one of the dependent variables, ϕ say, where $\phi = u, v, \tau_{xx}, \tau_{xy}$ or τ_{yy}. Particles that arrive at the four corner points of a control volume, $C_{i,j}$, associated with ϕ at time $t = t_{n+1}$ were located at the vertices of some cell at time $t = t_n$, which may be deformed. This cell is approximated by a quadrilateral $C^{*n}_{i,j}$, formed by joining the departure points by straight line segments (see Fig. 3).

Associated with each cell $C_{i,j}$ at each time $t_n = n\Delta t$, we introduce an approximation, denoted by $\phi^n_{i,j}$, to the cell average of $\phi(x, y, t_n)$, i.e.,

$$\phi^n_{i,j} \approx \frac{1}{\Delta x_i \Delta y_j} \int \int_{C_{i,j}} \phi(x, y, t_n) \mathrm{d}x \, \mathrm{d}y, \tag{28}$$

where

$$\Delta x_i = x_{i+1/2} - x_{i-1/2}, \quad \Delta y_j = y_{j+1/2} - y_{j-1/2}.$$

Thus, there are two stages to the numerical calculation at each time step:

(1) The departure points at time $t = t^n$ of each grid point on the reference grid are determined by using a particle following transformation. This initial-value problem is solved numerically at each grid point using Euler's method, for example.

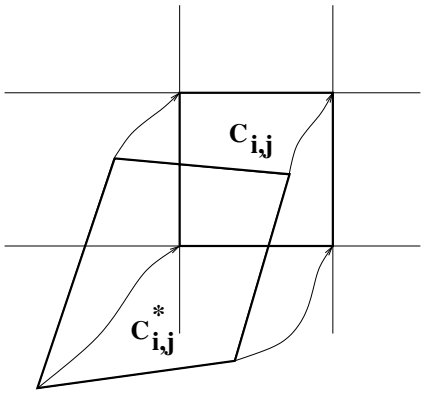

Fig. 3. The formation of the departure cell $C^{*}_{i,j}$ using the particle-following transformation to determine the vertices of this cell.

(2) The cell average values of ϕ^{*n} are determined from a knowledge of the cell average values of ϕ at time $t = t_n$ on the reference grid. These values are then inserted in Eqs. (25) and (27) in order to determine the values of velocity, pressure and stress at the new time step. This approximation is generated by means of an area-weighting technique that uses a weighted sum of the values of ϕ^{n} over the control volumes on the reference grid which overlap with cell $C^{*n}_{i,j}$ (see Fig. 4). Scroggs and Semazzi [22] developed a first-order area-weighting scheme that ensured global conservation of the scheme in a discrete sense. Phillips and Williams [18] generalised this to a second-order area-weighting scheme for determining the value of $\phi^{*n}_{i,j}$, in the form

$$\phi^{*n}_{i,j} = \frac{1}{\Delta x_i \Delta y_j} \sum_{I,J \in Z} \left[\omega^{I,J}_{i,j} (\phi^{n}_{I,J} - \alpha^{n}_{I,J} \bar{x}_{I,J} - \beta^{n}_{I,J} \bar{y}_{I,J}) + \int \int_{C^{*n}_{i,j} \cap C_{I,J}} \left(\alpha^{n}_{I,J} x + \beta^{n}_{I,J} y \right) \mathrm{d}x \, \mathrm{d}y \right], \tag{29}$$

where $\omega^{I,J}_{i,j}$ is the common area between $C^{*n}_{i,j}$ and $C_{I,J}$, i.e., the area of $C_{I,J} \cap C^{*n}_{i,j}$, Z is the set of indices of all the points in the computational domain and $\alpha_{i,j}$ and $\beta_{i,j}$ are central difference approximations to the fluxes. On a uniform grid we have

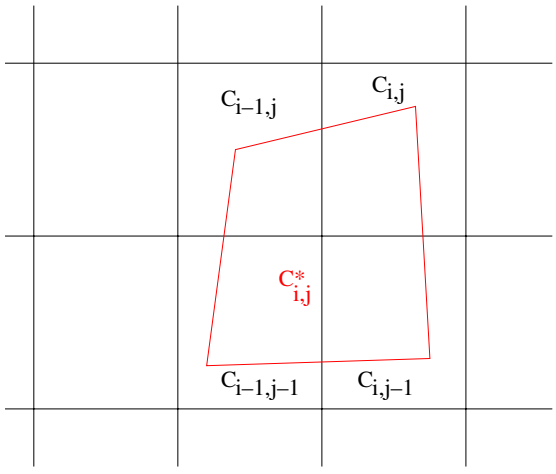

Fig. 4. A deformed control volume and the reference grid.

$$\alpha_{i,j}^n = \frac{\phi_{i+1,j}^n - \phi_{i-1,j}^n}{2\Delta x}, \qquad \beta_{i,j}^n = \frac{\phi_{i,j+1}^n - \phi_{i,j-1}^n}{2\Delta y}. \tag{30}$$

The point $(\bar{x}_{i,j}, \bar{y}_{i,j})$ is defined by

$$\bar{x}_{i,j} = \frac{1}{\Delta x_i \Delta y_j} \int\int_{C_{i,j}} x \,\mathrm{d}x \,\mathrm{d}y, \qquad \bar{y}_{i,j} = \frac{1}{\Delta x_i \Delta y_j} \int\int_{C_{i,j}} y \,\mathrm{d}x \,\mathrm{d}y. \tag{31}$$

This guarantees the global conservation properties of the scheme irrespective of the choice of approximation for the fluxes. If $C_{i,j}$ is convex this point will always lie in its interior. On a rectangular grid this is just the geometric centre of the cell.

5. Model Oldroyd-B flow problem

To test the spatial accuracy of the finite volume schemes described in this paper, a two-dimensional Cartesian model problem is solved on the unit square $[x_0, x_1] \times [y_0, y_1]$ with the prescribed velocity field given by

$$\mathbf{u} \equiv (x, -y). \tag{32}$$

Structured uniform meshes are used for both schemes. For the pure finite volume scheme quadrilateral (rectangular) finite volumes are used. For the hybrid scheme, a triangular FE-tessellation is constructed. Approximations are obtained on a series of meshes in order to determine the spatial accuracy of the schemes. Boundary conditions for the stress must be specified on the inflow boundaries of the domain $x = x_0$ and $y = y_1$. The initial conditions are taken as quiescent. We compute results for two domains obtained by changing the position of the top and bottom boundaries. These generate quite different flows. The first domain is $[1, 2] \times [1, 2]$ and the second is $[1, 2] \times [0.1, 1.1]$. Accuracy is measured by computing the maximum pointwise-errors in the approximations at the nodes of the finite volume mesh.

The component form of the Oldroyd-B equation with the above velocity field is

$$\begin{aligned} We\left(x\frac{\partial \tau_{xx}}{\partial x} - y\frac{\partial \tau_{xx}}{\partial y}\right) &= 2(1-\beta) + (2We-1)\tau_{xx}, \\ We\left(x\frac{\partial \tau_{xy}}{\partial x} - y\frac{\partial \tau_{xy}}{\partial y}\right) &= -\tau_{xy}, \\ We\left(x\frac{\partial \tau_{yy}}{\partial x} - y\frac{\partial \tau_{yy}}{\partial y}\right) &= -2(1-\beta) - (2We+1)\tau_{yy}. \end{aligned}$$

The true solution of this initial-value problem is of the form

$$\tau_i = a_i x^{c_i + d_i} y^{c_i} + b_i, \tag{33}$$

where the stress is represented as $(\tau_{xx}, \tau_{xy}, \tau_{yy}) \equiv (\tau_1, \tau_2, \tau_3)$, and the parameters in these representations are given by

$$b_1 = -\frac{2(1-\beta)}{(2We-1)}, \quad d_1 = 2 - \frac{1}{We},$$
$$b_2 = 0, \quad d_2 = -\frac{1}{We},$$
$$b_3 = -\frac{2(1-\beta)}{(2We+1)}, \quad d_3 = -2 - \frac{1}{We},$$

for $We < 1/2$. This is a condition that emerges on the normal stress component, τ_{xx}, similar to that observed in steady uniaxial extension. For the pressure to be compatible, the following relationships must hold between the coefficients a_i and c_i,

$$a_1 = -\frac{a_2 c_2}{c_1 + d_1}, \quad c_1 = c_2 - 1,$$
$$a_3 = -\frac{a_2(c_2 + d_2)}{c_3}, \quad c_3 = c_2 + 1.$$

The coefficients a_2 and c_2 can be chosen arbitrarily; we choose them to be unity.

We compare convergence behaviour of both finite volume approximations, in two domains described above, for $We = 0.4$ and $We = 0.1$, with $\beta = 1/9$. The time step was chosen to be $\Delta t = 0.002$ and the algorithms were terminated at steady-state when the relative maximum difference between the approximations at two successive time steps was less than 10^{-10}. The choice of time step was based on temporal stability and accuracy considerations. The stability considerations are based on the satisfaction of a CFL constraint. In addition the time step has to be sufficiently small to ensure that the temporal error is minimised. Based on equitable number of stress degrees of freedom, comparable finite volume meshes for the stress components are used as the basis of comparison of the two schemes (two triangular subcells of the hybrid scheme form a single rectangle in the pure FV scheme). For example, subsuming two triangles within a single rectangle, a $2n \times 2n$ mesh for the FE/FV scheme corresponds to an $n \times n$ finite element mesh. The relative errors, $E(h)$, in the components of the extra-stress tensor in the infinity norm are provided in Tables 1–4 for $We = 0.4$ and $We = 0.1$ over domains 1 and 2, where

$$E(h) = \frac{\|\tau_i - \tau_i^h\|_\infty}{\|\tau_i\|_\infty}. \tag{34}$$

Domain 2 is included, since in this geometry, the velocity is almost parallel to the bottom boundary. This situation can give rise to a deterioration in accuracy for some schemes. The order of approximation of the schemes is estimated using the formula

$$p = \frac{\ln(E(h)/E(h/2))}{\ln 2}, \tag{35}$$

Table 1
Mesh dependence of $E(h)$ for the model Oldroyd-B problem in domain 1 for $We = 0.4$

Mesh	FE/FV			SLFV		
	τ_{xx}	τ_{xy}	τ_{yy}	τ_{xx}	τ_{xy}	τ_{yy}
8×8	5.34×10^{-5}	4.20×10^{-4}	6.16×10^{-4}	6.01×10^{-4}	2.01×10^{-4}	3.60×10^{-4}
16×16	1.05×10^{-5}	1.10×10^{-4}	1.68×10^{-4}	1.11×10^{-5}	4.35×10^{-5}	7.81×10^{-5}
32×32	1.87×10^{-6}	2.31×10^{-5}	3.94×10^{-5}	2.01×10^{-6}	8.85×10^{-6}	1.62×10^{-5}
64×64	2.94×10^{-7}	4.09×10^{-6}	7.61×10^{-6}	3.35×10^{-7}	1.75×10^{-6}	2.72×10^{-6}

Table 2
Mesh dependence of $E(h)$ for the model Oldroyd-B problem in domain 2 for $We = 0.4$

Mesh	FE/FV			SLFV		
	τ_{xx}	τ_{xy}	τ_{yy}	τ_{xx}	τ_{xy}	τ_{yy}
8×8	3.56×10^{-5}	1.30×10^{-3}	6.94×10^{-4}	5.43×10^{-5}	9.98×10^{-5}	4.80×10^{-4}
16×16	5.23×10^{-6}	3.15×10^{-4}	1.79×10^{-4}	9.85×10^{-6}	2.33×10^{-5}	9.97×10^{-5}
32×32	7.09×10^{-7}	7.82×10^{-5}	4.69×10^{-5}	1.65×10^{-6}	5.09×10^{-6}	1.95×10^{-5}
64×64	1.03×10^{-7}	1.90×10^{-5}	1.22×10^{-5}	2.65×10^{-7}	1.06×10^{-6}	3.71×10^{-6}

Table 3
Mesh dependence of $E(h)$ for the model Oldroyd-B problem in domain 1 for $We = 0.1$

Mesh	FE/FV			SLFV		
	τ_{xx}	τ_{xy}	τ_{yy}	τ_{xx}	τ_{xy}	τ_{yy}
8×8	1.04×10^{-3}	1.24×10^{-2}	1.01×10^{-2}	4.58×10^{-4}	8.63×10^{-4}	9.85×10^{-4}
16×16	3.97×10^{-4}	6.17×10^{-3}	5.59×10^{-3}	7.99×10^{-5}	2.15×10^{-4}	2.34×10^{-4}
32×32	1.09×10^{-4}	1.89×10^{-3}	1.89×10^{-3}	1.31×10^{-5}	4.91×10^{-5}	5.41×10^{-5}
64×64	2.23×10^{-5}	4.16×10^{-4}	4.49×10^{-4}	2.08×10^{-6}	1.04×10^{-5}	1.22×10^{-5}

Table 4
Mesh dependence of $E(h)$ for the model Oldroyd-B problem in domain 2 for $We = 0.1$

Mesh	FE/FV			SLFV		
	τ_{xx}	τ_{xy}	τ_{yy}	τ_{xx}	τ_{xy}	τ_{yy}
8×8	7.93×10^{-4}	9.99×10^{-3}	9.82×10^{-3}	3.88×10^{-4}	9.91×10^{-4}	7.35×10^{-4}
16×16	2.45×10^{-4}	2.59×10^{-3}	3.18×10^{-3}	9.12×10^{-5}	2.49×10^{-4}	1.82×10^{-4}
32×32	5.03×10^{-5}	7.05×10^{-4}	9.17×10^{-4}	1.77×10^{-5}	5.83×10^{-5}	4.15×10^{-5}
64×64	8.32×10^{-6}	1.52×10^{-4}	1.99×10^{-4}	3.01×10^{-6}	1.22×10^{-5}	9.51×10^{-6}

and information obtained on the finest two meshes, that is, we take $h = 1/32$. Following this procedure yields the data gathered in Table 5. The order of convergence of both FE/FV and SLFV schemes is two at least, in fact, lying between two and three. We observe that there is a degradation in accuracy for both schemes across all stress components on domain 2, with the exception of τ_{xx} for the SLFV scheme. This reflects the fact that this is a more severe problem setting, with sharper aspects of the solution approximating the boundaries. In Figs. 5 and 6 for $We = 0.4$, the behaviour of $E(h)$ is displayed as function of h, for the two schemes and each of the stress components, in domains 1 and 2, respectively. In Fig. 5 we observe

Table 5
Estimates of the order of spatial convergence of the FE/FV and SLFV schemes for $We = 0.4$ and $We = 0.1$ in domains 1 and 2

We	Domain	FE/FV			SLFV		
		τ_{xx}	τ_{xy}	τ_{yy}	τ_{xx}	τ_{xy}	τ_{yy}
0.4	1	2.67	2.50	2.37	2.58	2.34	2.57
0.4	2	2.78	2.04	1.94	2.64	2.26	2.39
0.1	1	2.29	2.18	2.07	2.65	2.24	2.15
0.1	2	2.60	2.22	2.20	2.56	2.26	2.13

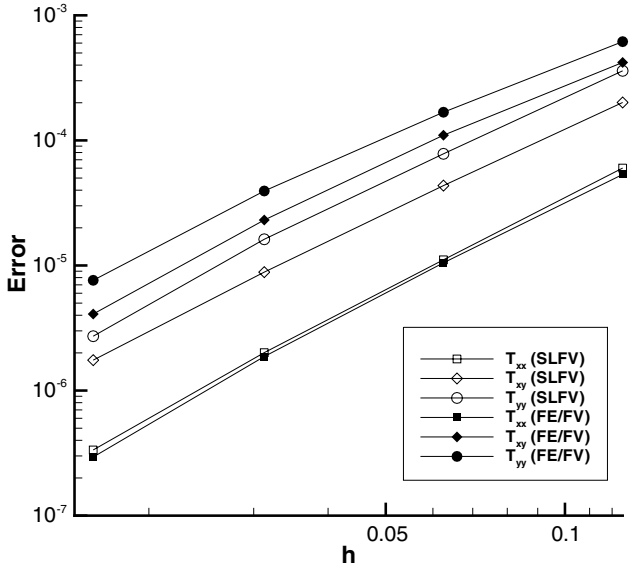

Fig. 5. Dependence of the error on h for $We = 0.4$ in domain 1.

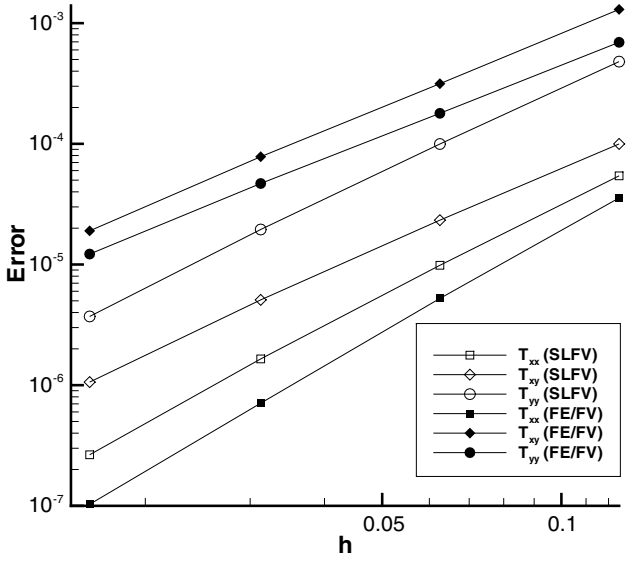

Fig. 6. Dependence of the error on h for $We = 0.4$ in domain 2.

almost $O(h^{2.5})$ convergence for all components for both SLFV and FE/FV schemes. The level of errors for τ_{xx} are the same for both schemes, whilst the levels of error are lower for the remaining components with the SLFV in contrast to the FE/FV scheme. Note, that the absolute value of τ_{xx} is greater than that for the other components in this particular problem. Moreover, the analytical solution for τ_{xx} is independent of y. In Fig. 6 the level of error for τ_{xx} is different for the two schemes. The same trends are observed for the other stress components as those shown in Fig. 5. Here, the asymptotic behaviour of the approximation error for

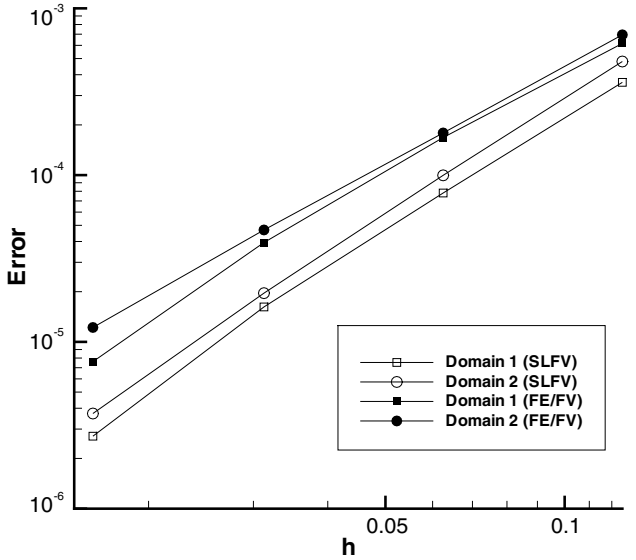

Fig. 7. Dependence of the error in T_{yy} on h for $We = 0.4$.

τ_{xx} is $O(h^{2.78})$ and $O(h^{2.64})$ for FE/FV and SLFV, respectively. To proceed with further comparisons we select a single representative stress component, τ_{yy} (the more severe). In Fig. 7 we compare the behaviour of the error $E(h)$ for the stress component τ_{yy}. The level of error for this component is lower for the SLFV approximation than for the FE/FV approximation. This can be explained by the particular properties of the grids used in the two schemes for the approximation of the stress components: subtriangles in the FE/FV scheme and a staggered rectangular grid in the SLFV scheme.

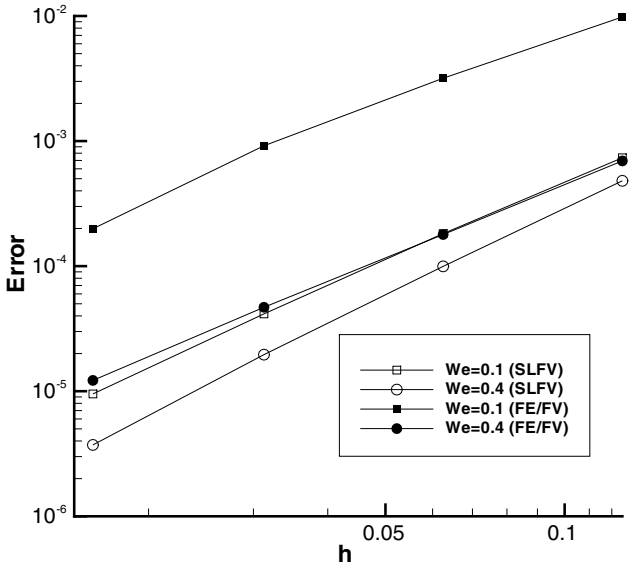

Fig. 8. Dependence of the error in T_{yy} on h in domain 2.

To examine the behaviour of the approximation error with respect to the Weissenberg number we contrast the behaviour of the error $E(h)$ against h in Fig. 8 for the two schemes with $We = 0.1$ and $We = 0.4$, over domain 1 and again selecting the stress component τ_{yy}. We observe that the level of accuracy for $We = 0.1$ is higher than for that $We = 0.4$. This is due to the fact that the absolute value of τ_{yy} for $We = 0.1$ is larger than that for $We = 0.4$. Once again, the desired $O(h^2)$ convergence is obtained.

6. Unsteady Poiseuille flow in a planar channel

Consider the transient flow development of an Oldroyd-B fluid in a planar channel, commencing from a state of rest when a constant pressure-gradient is applied. This is a physically realistic problem when instigated from quiescent conditions. For the Oldroyd-B fluid, an analytical solution to this problem has been derived by Waters and King [25]. For example, the velocity components can be written in the form

$$u(y,t) = U\left[A(y) - 32\sum_{n=1}^{\infty}\frac{\sin(Ny)}{N^3}\exp\left(-\frac{\alpha_N t}{2S_1}\right)G_N(t)\right] \tag{36}$$

and $v(y,t) = 0$, where $A(y) = 4(1-y)y$, $N = (2n-1)\pi$ and

$$G_N(t) = \cosh\left(\frac{\beta_N t}{2S_1}\right) + \left[\frac{1+N^2(S_2-2S_1)}{\beta_N}\right]\sinh\left(\frac{\beta_N t}{2S_1}\right), \tag{37}$$

$$S_1 = \frac{We}{Re}, \quad S_2 = \beta S_1, \quad \alpha_N = 1 + S_2N^2, \quad \beta_N = \sqrt{(1+S_2N^2)^2 - 4S_1N^2}. \tag{38}$$

The stress components are given by

$$\begin{aligned}\tau_{xx} = {} & 2ReC_{xy}(S_1,y)\left[A'(y)\exp\left(-\frac{t}{S_1}\right) - 32\sum_{n=1}^{\infty}\frac{\cos(Ny)}{N^2}I_N(S_1,t)\right] \\ & + 2ReA'(y)(1-\beta)\left[S_1A'(y) - 32\sum_{n=1}^{\infty}\frac{\cos(Ny)}{N^2}H_N(S_1,t)\right] - \frac{64ReA'(y)(1-\beta)}{S_1}\sum_{m=1}^{\infty}\frac{\cos(My)}{M^2}J_M(S_1,t) \\ & + \frac{2048Re(1-\beta)}{S_1}\sum_{n,m=1}^{\infty}\frac{\cos(Ny)}{N^2}\frac{\cos(My)}{M^2}K_{NM}(S_1,t) + C_{xx}(S_1,y)\exp\left(-\frac{t}{S_1}\right),\end{aligned} \tag{39}$$

$$\tau_{xy} = \frac{(1-\beta)}{S_1}\left[S_1A'(y) - 32\sum_{n=1}^{\infty}\frac{\cos(Ny)}{N^2}H_N(S_1,t)\right] + C_{xy}(S_1,y)\exp\left(-\frac{t}{S_1}\right), \tag{40}$$

$$\tau_{yy} = 0, \tag{41}$$

where $M = (2m-1)\pi$, and C_{xy} and C_{xx} are time-independent functions defined by the requirement that τ_{xy} and τ_{xx} are zero at $t = 0$, respectively. Details of the other coefficients are given in Carew et al. [3]. The boundary conditions on the velocity at inflow and outflow are taken to be the transient expressions determined by Waters and King [25]. Similarly, the analytical expressions for the extra-stress components are imposed at inflow. No-slip boundary conditions are imposed at the channel walls. The transient development of the stress can exhibit both overshoots and undershoots as it evolves towards the steady-state

solution. The problem has a smooth solution, being a pure transient shear flow, with a shear boundary layer at the channel walls and no shear along the centreline. There are no geometric singularities in the flow. Here, interest lies solely in determining the quality of the numerical solutions, evolved over time, and in detecting sensitivity to numerical instability for the algorithms under consideration.

For $\beta = 1/9$, the analytical solution displays overshoots and undershoots in the streamwise velocity component and the stress components, as *We* is increased from a value of zero to unity. As *We* is increased beyond unity, the velocity overshoot increases, whilst velocity undershoot and stress overshoot/undershoot are damped. Once *We* reaches 100 there is no velocity undershoot or stress overshoot/undershoot. Also of interest is the relative times taken for velocity and stress components to settle down to their steady-state values. For $We < 1$, velocity and stress components take approximately the same time to achieve such states. However, for $We \geqslant 1$, normal stress components take longer to attain their steady-state values as compared with velocity components and shear stress. Reproducing these features is a severe test of the time accuracy of any transient algorithm, given the different time-scales involved.

The *unstructured* 10×10 mesh employed for the hybrid FE/FV scheme, see Fig. 9, teases out the nuances of FD-upwinding and identifies sampled internal and boundary nodes for reference. The SLFV scheme is validated on a 10×10 rectangular equivalent, but *structured* mesh. The accuracy of the numerical solutions is judged from the ability to capture transient overshoots and undershoots (present in the analytical solution), alongside long-term steady-state response. The performance of the two schemes is investigated for $We = 1$ and for two values of β. When $\beta = 1/9$, the solvent contribution to the extra-stress tensor is small compared with that of the polymeric contribution. In this instance the analytical solution displays overshoots and undershoots in the velocity and extra-stress. When $\beta = 1/2$, the solvent and polymeric contributions to the extra-stress tensor are equally weighted. In this case, the axial velocity possesses a single overshoot before settling down to its steady state value. There is no overshoot in extra-stress. The time step is chosen to be $\Delta t = 10^{-2}$.

With $\beta = 1/9$, both schemes predict closely the transient response of the axial component of the velocity at a point, interior to the domain (see Fig. 10). The SLFV scheme slightly underpredicts the first peak and even more slightly overpredicts the first trough of the analytical solution. The relative error for the FE/FV scheme reaches its maximum at the second peak (1%) declining to 0.1% at the third peak whilst capturing the first peak and long-time behaviour within 0.04% of the analytical solution.

The transient stress also exhibits both overshoots and undershoots as it evolves towards a steady-state. At the boundary point, the maximum relative error for the normal stress T_{xx} is less than 4% (corresponding to first peak), which reduces to 0.3% at the steady state. Both schemes underpredict the analytical solution until around a time of $t = 6$ (see Fig. 11). At the interior point the hybrid FE/FV scheme overpredicts the first peak (less than 4% of the analytical solution), and then, underpredicts the solution, (see Fig. 12). However, the approximation remains in phase with the analytical solution. The SLFV scheme

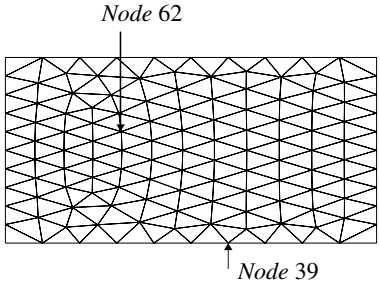

Fig. 9. Finite element 10×10 mesh.

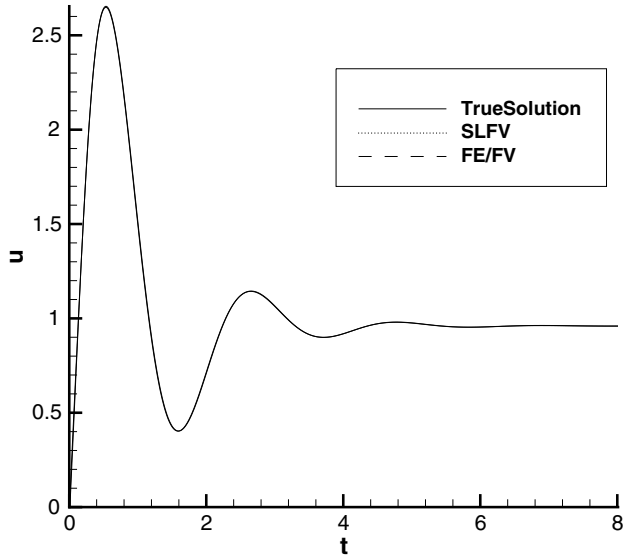

Fig. 10. Comparison of the transient development of the horizontal velocity component u with the finite volume approximations at an interior sampling point for $We = 1$ and $\beta = 1/9$.

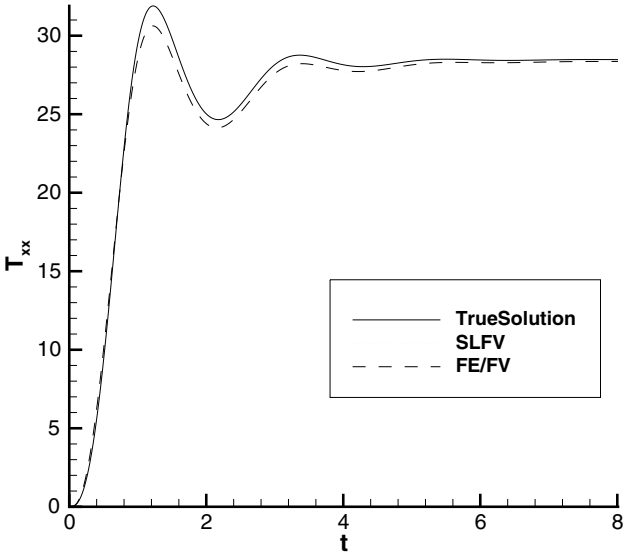

Fig. 11. Comparison of the transient development of the normal stress T_{xx} with the finite volume approximations at a boundary sampling point for $We = 1$ and $\beta = 1/9$.

underpredicts the first peak, overpredicts the first trough, lagging slightly out-of-phase, until agreeing with the analytical solution at around $t = 5$.

For $\beta = 1/2$, both schemes are observed to capture the transient response accurately (see Figs. 13–15). The SLFV scheme slightly underpredicts the peak in the axial component of the velocity. For the normal stress component, T_{xx}, the SLFV approximation lags slightly behind the analytical solution,

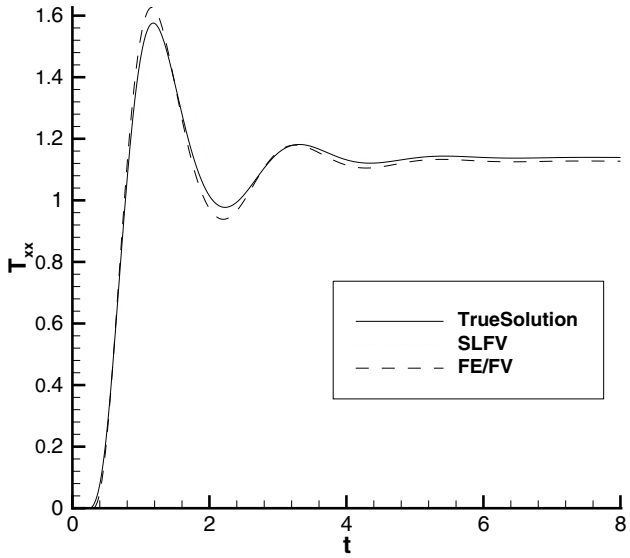

Fig. 12. Comparison of the transient development of the normal stress T_{xx} with the finite volume approximations at an interior sampling point for $We = 1$ and $\beta = 1/9$.

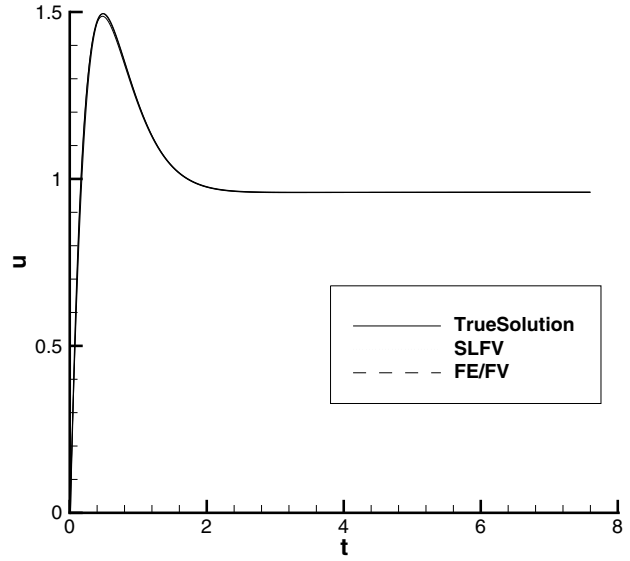

Fig. 13. Comparison of the transient development of the horizontal velocity component u with the finite volume approximations at an interior sampling point for $We = 1$ and $\beta = 1/2$.

whilst the hybrid FE/FV remain in phase. In Figs. 16–19, we display the behaviour of the shear stress for $\beta = 1/9$ and $\beta = 1/2$ at boundary and interior sampling points. Identical sample points are selected as for the normal stress component. The FE/FV approximation matches the analytical solution

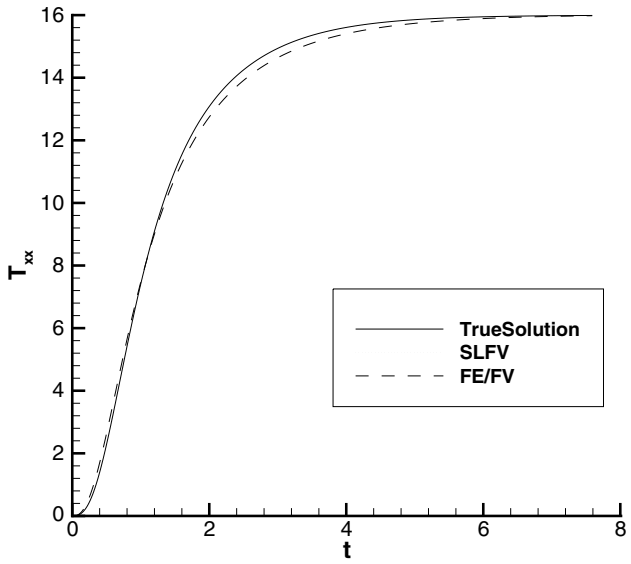

Fig. 14. Comparison of the transient development of the normal stress T_{xx} with the finite volume approximations at a boundary sampling point for $We = 1$ and $\beta = 1/2$.

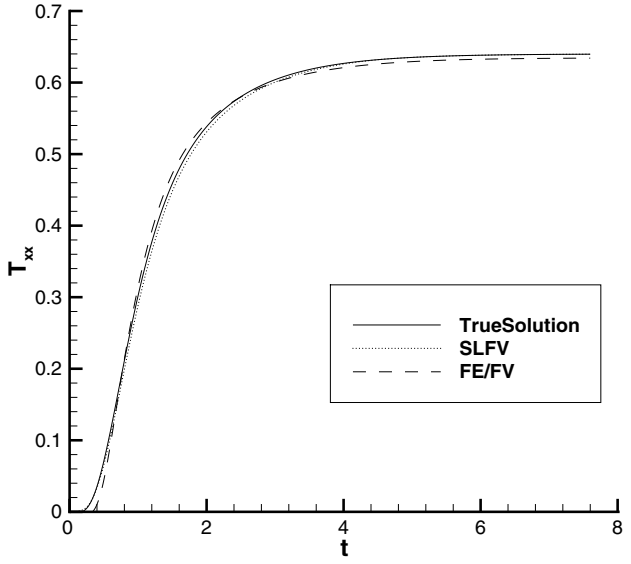

Fig. 15. Comparison of the transient development of the normal stress T_{xx} with the finite volume approximations at an interior sampling point for $We = 1$ and $\beta = 1/2$.

throughout the time period, albeit with a small undershoot at the first peak (see Figs. 16 and 17). This is a result of the correspondence between the linear nature of the shear stress and the linear interpolation of the stress approximation employed in the FE/FV scheme. There is also an improvement in

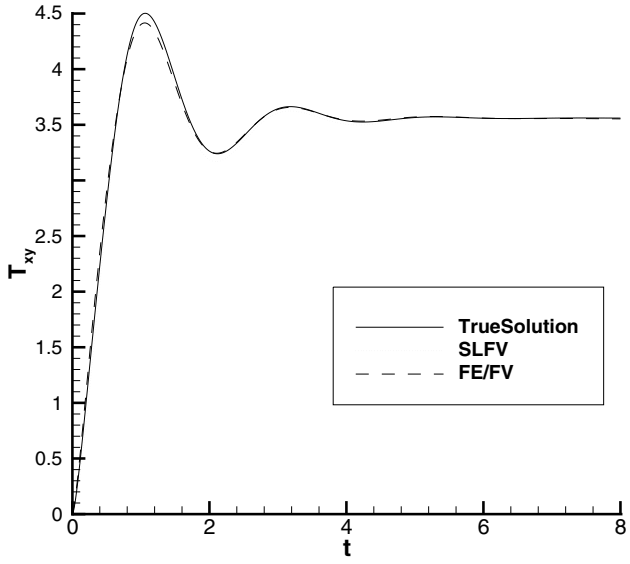

Fig. 16. Comparison of the transient development of the shear stress T_{xy} with the finite volume approximations at a boundary sampling point for $We = 1$ and $\beta = 1/9$.

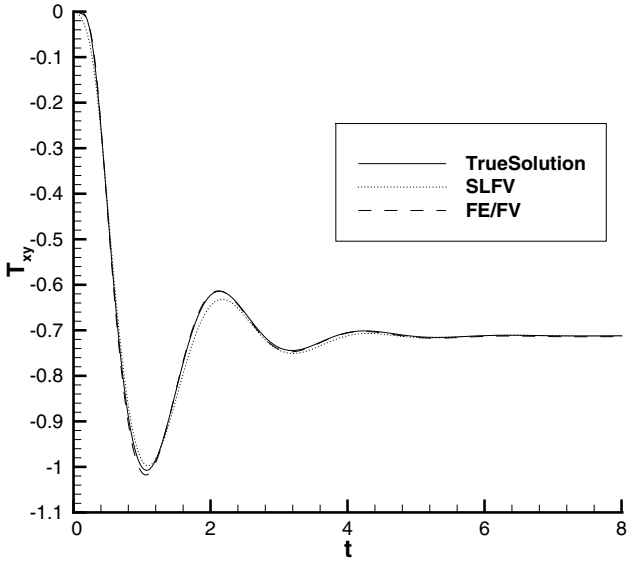

Fig. 17. Comparison of the transient development of the shear stress T_{xy} with the finite volume approximations at an interior sampling point for $We = 1$ and $\beta = 1/9$.

the SLFV approximation in terms of better phase-matches compared with the corresponding plots for the normal stress at the same locations.

Finally, we note that the analytical solution is smoother for $\beta = 1/2$ than for $\beta = 1/9$. For example, the horizontal component of velocity possesses a single peak before decaying monotonically to its steady state

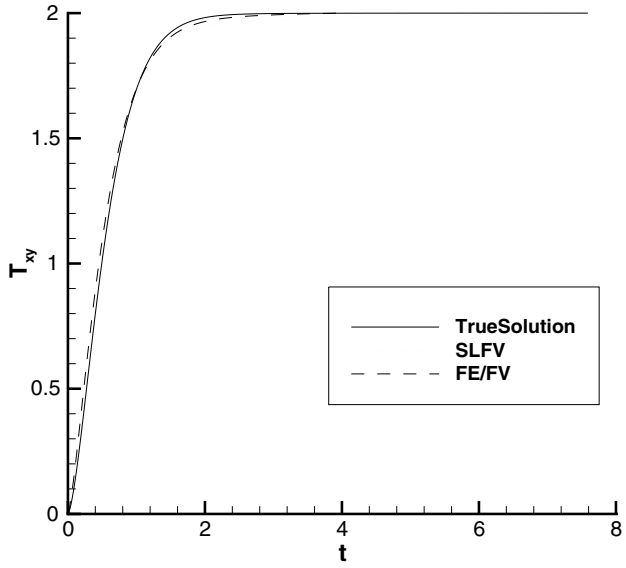

Fig. 18. Comparison of the transient development of the shear stress T_{xy} with the finite volume approximations at a boundary sampling point for $We = 1$ and $\beta = 1/2$.

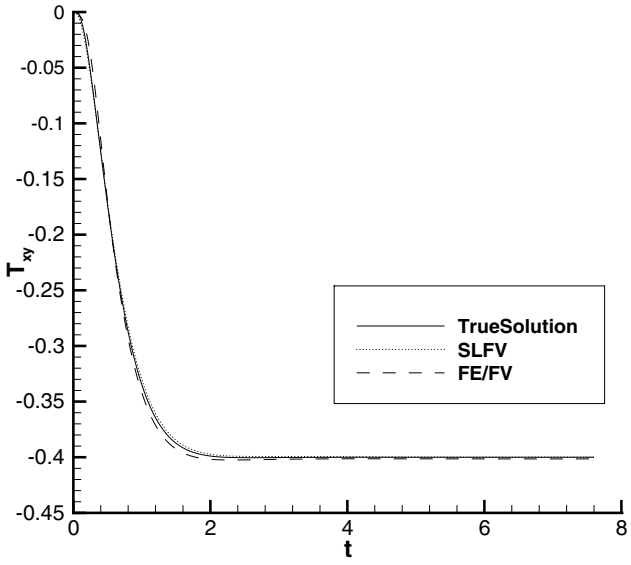

Fig. 19. Comparison of the transient development of the shear stress T_{xy} with the finite volume approximations at an interior sampling point for $We = 1$ and $\beta = 1/2$.

value (see Fig. 10) and the shear stress behaves monotonically (see Figs. 18 and 19) for $\beta = 1/2$. Accordingly, the quality of the approximations is improved compared with the corresponding behaviour for $\beta = 1/9$.

7. Conclusions

In this paper we have presented and analysed two contrasting finite volume strategies for solving viscoelastic flow problems. The schemes have been constructed to be second-order in space and this has been demonstrated by means of a model problem, based on the Oldroyd-B constitutive equation. Stability for the hybrid FE/FV scheme (reaching high Weissenberg number solutions) has been achieved by a combination of a subgrid for the stress and a consistent treatment of flux and source terms in the momentum equation using fluctuation distribution and median-dual-cells. Stability for the pure finite volume schemes has been achieved using a semi-Lagrangian treatment of the convective terms in the constitutive equation in which a high-order area-weighting technique is used to evaluate contributions at the previous time step. The transient behaviour of such schemes has been investigated by considering the unsteady Poiseuille flow of an Oldroyd-B fluid in a planar channel. The performance of both FV-implementations on these case studies provides us with the confidence to apply them to complex flows of viscoelastic fluids. At the next stage, one may take advantage of the independent scheme derivations to combine ideas from one scheme into another. So, for example, source term treatment may be adopted from hybrid FE/FV within SLFV, to progress to unstructured meshing. Likewise, semi-Lagrangian ideology may replace or complement flux term treatment within the hybrid FE/FV scheme.

References

[1] M. Aboubacar, M. Webster, A cell-vertex finite volume/element method on triangles for abrupt contraction viscoelastic flows, J. Non-Newtonian Fluid Mech. 98 (2001) 83–106.
[2] M.J. Bevis, M.S. Darwish, J.R. Whiteman, Numerical modelling of viscoelastic liquids using a finite volume method, J. Non-Newtonian Fluid Mech. 45 (1992) 311–337.
[3] E.O.A. Carew, P. Townsend, M.F. Webster, Taylor–Galerkin algorithms for viscoelastic flow: application to a model problem, Numer. Methods Partial Differential Equations 10 (1994) 171–190.
[4] M.S. Chandio, M.F. Webster, On consistency of cell-vertex finite-volume formulations for viscoelastic flow, in: D.M. Binding, N.E. Hudson, J. Mewis, J.-M. Piau, C.J.S. Petrie, P. Townsend, M.H. Wagner, K. Walters (Eds.), XIII Int. Cong. on Rheol., Cambridge, vol. 2, British Society of Rheology, Glasgow, 2000, pp. 208–210.
[5] H. Deconinck, P.L. Roe, R. Struijs, A multi-dimensional generalization of Roe's flux difference splitter for the Euler equations, Comput. Fluids 22 (1993) 215–222.
[6] J. Donea, A Taylor–Galerkin method for convective transport problems, Int. J. Numer. Methods Eng. 20 (1984) 101–119.
[7] M. Fortin, R. Pierre, On the convergence of the mixed method of Crochet and Marchal for viscoelastic flows, Comput. Methods Appl. Mech. Eng. 73 (1989) 341–350.
[8] M. Gerritsma, Time dependent numerical simulations of a viscoelastic fluid on a staggered grid, Ph.D. Thesis, University of Groningen, The Netherlands, 1996.
[9] R. Guénette, M. Fortin, A new mixed finite element method for computing viscoelastic flows, J. Non-Newtonian Fluid Mech. 60 (1995) 27–52.
[10] D.M. Hawken, H.R. Tamaddon-Jahromi, P. Townsend, M.F. Webster, A Taylor–Galerkin based algorithm for viscous incompressible flow, Int. J. Numer. Methods Fluids 10 (1990) 327–351.
[11] M.E. Hubbard, P.L. Roe, Multidimensional upwind fluctuation distribution schemes for scalar dependent problems, Int. J. Numer. Methods Fluids 33 (2000) 711–736.
[12] A. Jameson, D. Mavriplis, Finite volume solution of the two-dimensional Euler equations on a regular triangular mesh, AIAA 24 (1986) 611–618.
[13] J. Van Kan, A second-order accurate pressure-correction scheme for viscous incompressible flow, SIAM J. Sci. Statist. Comput. 7 (3) (1986) 870–891.
[14] J.M. Marchal, M.J. Crochet, A new mixed finite element method for calculating viscoelastic flow, J. Non-Newtonian Fluid Mech. 26 (1987) 77–114.
[15] G. Mompean, M. Deville, Unsteady finite volume simulation of Oldroyd-B fluid through a three-dimensional planar contraction, J. Non-Newtonian Fluid Mech. 72 (1997) 253–279.
[16] K.W. Morton, P.I. Crumpton, J.A. MacKenzie, Cell vertex methods for inviscid and viscous flows, Comput. Fluids 22 (1993) 91–102.

[17] R.G. Owens, T.N. Phillips, Computational Rheology, Imperial College Press, London, 2002.
[18] T.N. Phillips, A.J. Williams, Conservative semi-Lagrangian finite volume schemes, Numer. Methods Partial Differential Equations 17 (2001) 403–425.
[19] T.N. Phillips, A.J. Williams, Viscoelastic flow through a planar contraction using a semi-Lagrangian finite volume method, J. Non-Newtonian Fluid Mech. 87 (1999) 215–246.
[20] D. Rajagopalan, R.C. Armstrong, R.A. Brown, Finite element methods for calculation of steady, viscoelastic flow using constitutive equation with a Newtonian viscosity, J. Non-Newtonian Fluid Mech. 36 (1990) 159–192.
[21] G.P. Sasmal, A finite volume approach for calculation of viscoelastic flow through an abrupt axisymmetric contraction, J. Non-Newtonian Fluid Mech. 56 (1995) 15–47.
[22] J.S. Scroggs, F.H.M. Semazzi, A conservative semi-Lagrangian method for multidimensional fluid dynamics applications, Numer. Methods Partial Differential Equations 11 (1995) 445–452.
[23] H.R. Tamaddon-Jahromi, M. Aboubacar, M.F. Webster, Time-dependent algorithms for viscoelastic flow – finite element/volume schemes, Numer. Methods Partial Differential Equations (2002), submitted, see Tech. Rep. Univ. Wales Swansea CSR 11-2002.
[24] P. Wapperom, M.F. Webster, Simulation for viscoelastic flow by a finite volume/element method, Comput. Methods Appl. Mech. Eng. 180 (1999) 281–304.
[25] N.D. Waters, M.J. King, Unsteady flow of an elastico-viscous liquid, Rheol. Acta, 9 (1970) 345–355.
[26] N.P. Weatherill, A method for generating irregular computational grids in multiply connected planar domains, Int. J. Numer. Methods Fluids 8 (1988) 181–197.
[27] M.F. Webster, P. Wapperom, A second-order hybrid finite-element/volume method for viscoelastic flows, J. Non-Newtonian Fluid Mech. 79 (1998) 405–431.
[28] S.-C. Xue, N. Phan-Thien, R.I. Tanner, Three dimensional numerical simulation of viscoelastic flows through planar contractions, J. Non-Newtonian Fluid Mech. 74 (1998) 195–245.
[29] J.Y. Yoo, Y. Na, A numerical study of the planar contraction flow of a viscoelastic fluid using the SIMPLER algorithm, J. Non-Newtonian Fluid Mech. 30 (1991) 89–106.
[30] O.C. Zienkiewicz, K. Morgan, J. Peraire, M. Vandati, R. Löhner, Finite elements for compressible gas flow and similar systems, in: Proc. of the 7th Int. Conf. Comput. Meth. Appl. Sci. Eng., Versailles, France, 1985.